Journal of Sound and Vibration (1999) **226**(4), 625–644
Article No. jsvi.1999.2309, available online at http://www.idealibrary.com on IDEAL®

DYNAMIC SIMULATION OF A BIMODAL ULTRASONIC MOTOR BY NEW HYBRID LAPLACE TRANSFORM/FINITE ELEMENT METHOD

R.-F. FUNG AND C. R. TSENG

Department of Mechanical Engineering, Chung Yuan Christian University, Chung-Li, Taiwan, 32023, Republic of China

AND

C.-M. YAO

National Center for High-Performance Computing, Hsinchu, Taiwan, Republic of China

(*Received* 31 *August* 1998, *and in final form* 26 *March* 1999)

A new hybrid Laplace transform/finite element method is proposed to solve the dynamic problem of a bimodal ultrasonic motor, which used a piezoelectric beam to drive the rotor. Two modes, longitudinal and flexural, of the piezoelectric beam are simultaneously excited by only one power amplifier. A set of differential equations is derived by finite element formulation for this oscillating beam. A proper similarity transform technique is used to decouple the Laplace transformed equations governing the vibration of the beam without contact and to make the inverse Laplace transformation easier. The contact problem between the beam and the rotor is also formulated and numerically solved. It is found that the simulation results obtained by using this hybrid method are almost identical with those by the Runge–Kutta method, but the former is able to avoid an excessive amount of computation time. Some important factors affecting the behavior of this motor are studied, including structure design, amplitude of input voltage, phase displacement, exciting frequency, gap between beam tip and rotor, and contact phenomena.

1. INTRODUCTION

In previous studies, the hybrid Laplace transform/finite difference method [1, 2] and the Laplace transform/finite element method [3, 4] were proposed to solve mainly for linear transient heat-conduction problems. A new hybrid Laplace transform/finite element method was applied to solve two- and three-dimensional linear transient heat conduction problems [5, 6]. For non-linear problems, the non-linear terms in the governing equations were linearized by Taylor's series expansion [7] in order to apply this method. Recently, the quasi-static and dynamic response of a linear viscoelastic beam has been solved numerically by using the hybrid Laplace transform/finite element method [8]. The main difficulty in applying the hybrid method is to solve a set of linear equations with complex-number

0022-460X/99/390625 + 20 $30.00/0

coefficients formed by the Laplace transform and then to take the inverse Laplace transform. The numerical inversion form of the Laplace transform can be written as trigonometric integrals by using the Durbin method [9]. In order to avoid the numerically induced oscillations in the solutions, the inverse Laplace transform method of Honing and Hirdes [10] was proposed, where 60 or 100 terms of Fourier series expansion must be taken. Therefore it takes excessive computer time.

Fleischer *et al.* [11–13] developed a new motor, in which a bi-directional piezoelectric ultrasonic motor is operated with only a single input voltage and thus only one power amplifier is needed. This driving voltage excites simultaneously the longitudinal and flexural oscillation modes of a beam resonator. This type of ultrasonic motor is called the bimodal motor. The dynamic characteristic of this motor is studied in this paper.

The configuration of the bimodal motor is shown in Figure 1. The piezoelectric beam in this model is composed of a steel beam, three PZT pieces and an aluminum beam. The mathematical model is derived based on the general formulations of constitutive laws in piezoelectric materials [14, 15] and isotropic materials, and the finite element method is applied to discretize the space domain. After deriving the geometry constraint at the contact point and applying the Lagrange multiplier method, the governing differential-algebraic equations for the contact behavior between the stator beam and the rotor are formulated and solved numerically. The new hybrid Laplace transform/finite element method [5, 6] is employed to solve the equations governing the vibrations of a bimodal ultrasonic motor without contact. A proper similarity transform technique is used to decoupled the Laplace transformed equations and to make the inverse transform easier. The method can save a considerable amount of computation time compared with other methods, such as the Runge–Kutta method, in which the numerical accuracy is greatly dependent on integration time step. Some important design factors are studied which include structure design, amplitude of input voltage, phase displacement, exciting frequency, gap between stator and rotor and contact phenomena.

2. FORMULATIONS OF PHYSICAL MODEL

2.1. FINITE ELEMENT FORMULATION OF STATOR BEAM

The model of the bimodal ultrasonic motor consists of a piezoelectric stator and a rotor as shown in Figure 1. The stator beam is divided into four regions with total length l_t. Region 1 of the beam is made of steel with length l_s. Region 2 is the piezoceramics with length l_l, used for the longitudinal oscillation. Two pieces of piezoceramics partitioned up and down form region 3 with length l_f and are used for flexural oscillation by placing piezoceramics in the opposite polarization direction. Region 4 of the beam is made of aluminum with length l_a which may contact with the rotor. The global co-ordinate system OXY is located at the fixed root of the stator. The beam is modelled as a Timoshenko beam and the Lagrangian equations are used to derive the equations of motion of the system.

The kinetic energy of the stator beam for each region can be expressed as

$$K_i = \frac{1}{2}\int_{V_i} \rho_i \mathbf{R}_t(x, y, t)\cdot \mathbf{R}_t(x, y, t)\,\mathrm{d}V_i,\ i = 1, 2, \ldots, 4, \tag{1}$$

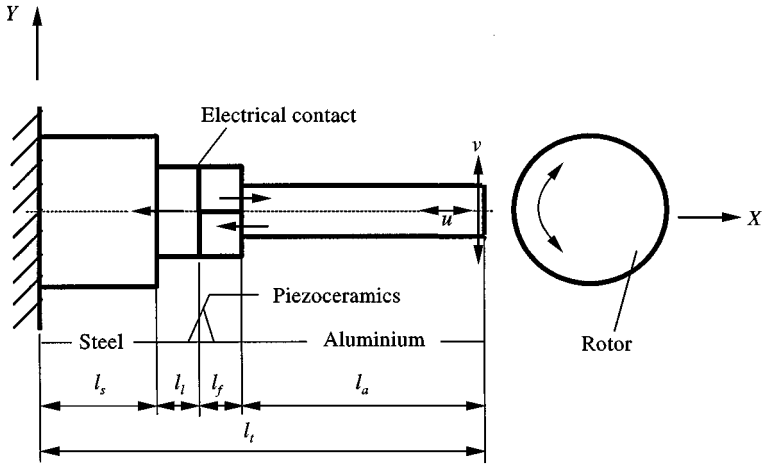

Figure 1. Schematic diagram of the bimodal piezomotor driven with a longitudinal mode and a flexural mode. Big arrows indicate directions of polarization of the piezoceramics.

where $\mathbf{R}_t$ is the velocity of any point on the beam at the position $\mathbf{R}$, ρ_i is the mass density and V_i is the volume for the region i of the beam.

The potential energy for regions 2 and 3 of the piezoceramics can be expressed as

$$U_1 = \frac{1}{2}\int_{V_p} (\{S\}^{\mathrm{T}}[c^E]\{S\} - \{S\}^{\mathrm{T}}[e]\{E\} - \{E\}^{\mathrm{T}}[e]^{\mathrm{T}}\{S\} - \{E\}^{\mathrm{T}}[\varepsilon^s]\{E\})\,\mathrm{d}V, \quad (2)$$

where c^E_{ijkl} is the elastic coefficient at a constant electric field, e_{ijk} is the piezoelectric coefficient and ε^s_{ik} is the dielectric coefficient at a constant elastic stress, S_{ij} is the small strain component, E_k is the electric field and V_p denotes the volume of piezoceramics. The potential energy for regions 1 and 4 of the steel and aluminum is

$$U_2 = \frac{1}{2}\int_{V_s} \{S\}^{\mathrm{T}}[c^E]\{S\}\,\mathrm{d}V, \quad (3)$$

where V_S is the volume for steel and aluminum parts.

The components of the linear Lagrangian strain for the Timoshenko beam modal are

$$S_{11} = u_x - y\psi_x, \qquad S_{22} = 0, \qquad S_{12} = S_{21} = \tfrac{1}{2}(v_x - \psi), \quad (4)$$

where u and v represent the axial and transverse displacements of the stator beam, respectively, ψ is the rotating angle of the cross-section and the electric field in the piezoceramics part of the beam is

$$E_1 = -\phi_x, \quad (5)$$

where ϕ is the electric potential.

The virtual works in the mechanical and electrical domains are, respectively,

$$\delta W_F = \mathbf{F}^*_F \cdot \delta\mathbf{R}(l_t, 0, t) = -P\delta u(l_t, t) + Q\delta v(l_t, t), \quad (6)$$

$$\delta W_Q = -\int_A \delta\phi\,\{v_\phi\}^{\mathrm{T}}\{D_i\}\,\mathrm{d}A, \quad (7)$$

where $\mathbf{F}_F^* = -P\mathbf{i} + Q\mathbf{j}$ is the external force applied at $x = l_t$. The forces P and Q are the axial compressive force and transverse force, respectively. $\{v_\phi\}$ is the vector of surface direction cosines and $\{D_i\}$ is electric displacement.

By applying the finite element method, the stator is decomposed into many Timoshenko beam elements. The nodal degrees of freedom of a beam element are composed of the axial displacement u, transverse displacement v and angle ψ. For the piezoceramics beam element, each node has an additional degree of freedom of electric potential ϕ. The displacement v and slope ψ of the beam element can be described by using the cubic polynomial functions and the deflection u and electric potential ϕ by using the linear polynomial functions.

Following the standard formulation of the finite element method for equations (1)–(3), one obtains the kinetic energy and potential energy for each beam element as

$$K_e = \tfrac{1}{2}\dot{\mathbf{q}}_u^{\mathrm{T}}[m]\dot{\mathbf{q}}_u, \tag{8}$$

$$U_{1e} = \tfrac{1}{2}(\mathbf{q}_u^{\mathrm{T}}[k_{uu}]\mathbf{q}_u + \mathbf{q}_u^{\mathrm{T}}[k_{u\phi}]\mathbf{q}_\phi + \mathbf{q}_\phi^{\mathrm{T}}[k_{\phi u}]\mathbf{q}_u - \mathbf{q}_\phi^{\mathrm{T}}[k_{\phi\phi}]\mathbf{q}_\phi), \tag{9}$$

$$U_{2e} = \tfrac{1}{2}\mathbf{q}_u^{\mathrm{T}}[k_{uu}]\mathbf{q}_u, \tag{10}$$

where $[m]$, $[k_{uu}]$, $[k_{u\phi}]$, $[k_{\phi u}]$ and $[k_{\phi\phi}]$ are element matrices for each region of the stator beam element. A detailed formulation of the above equations can be found in reference [16].

Hamilton's principle without constraint is

$$\int_{t_1}^{t_2}\left(\sum_{i=1}^{N_e}\delta L_i + \delta W_F + \delta W_Q\right)\mathrm{d}t = 0, \tag{11}$$

where N_e is the total number of elements of the piezoelectric beam and $L_i = T_i - U_i$ is Lagrangian function of each element.

By substituting equations (8–10) into equation (11), performing calculus of variation, assembling all of the element equations and applying the boundary conditions $u_l = v_l = \psi_l = 0$ at the fixed end, a set of global ordinary differential equations of the system can be obtained:

$$\begin{bmatrix}\mathbf{M}_{uu} & 0\\ 0 & 0\end{bmatrix}\begin{Bmatrix}\ddot{\mathbf{Q}}_u\\ \ddot{\mathbf{Q}}_\phi\end{Bmatrix} + \begin{bmatrix}\mathbf{K}_{uu} & \mathbf{K}_{u\phi}\\ \mathbf{K}_{u\phi}^{\mathrm{T}} & -\mathbf{K}_{\phi\phi}\end{bmatrix}\begin{Bmatrix}\mathbf{Q}_u\\ \mathbf{Q}_\phi\end{Bmatrix} = \begin{Bmatrix}\mathbf{F}_F\\ \mathbf{F}_Q\end{Bmatrix}, \tag{12}$$

where $\mathbf{Q}_u = \{u_2, v_2, \psi_2, \ldots, u_{N_e+1}, v_{N_e+1}, \psi_{N_e+1},\}^{\mathrm{T}}$ is the nodal displacement vector, $\mathbf{Q}_\phi = \{\phi_1, \ldots, \phi_{m2+m3+1}\}^{\mathrm{T}}$ is the electric potential vector, where m_2 and m_3 are the element numbers in regions 2 and 3, respectively, $\mathbf{M}_{uu}$ is the mass matrix, $\mathbf{K}_{uu}$, $\mathbf{K}_{u\phi}$ and $\mathbf{K}_{\phi\phi}$ are mechanical, piezoelectric and dielectric stiffness matrices, respectively. $\mathbf{F}_F$ is the mechanical force vector and $\mathbf{F}_Q$ is the electrical charge vector.

2.2. CONDENSATION OF SYSTEM EQUATIONS

In the bimodal motor design, one of the goals is to have a beam resonator such that one of its bending natural frequency is two times its axial natural frequency

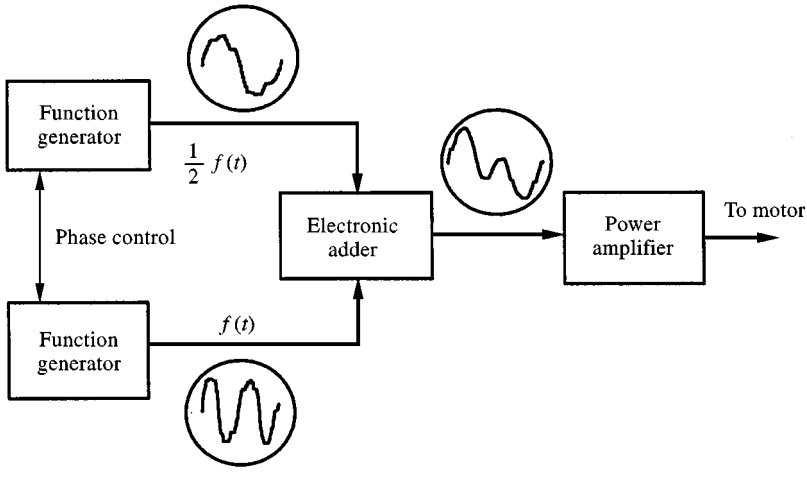

Figure 2. Block diagram of electrical driving circuit.

[13]. This bimodal motor is driven by an applied voltage shown in Figure 2. As an applied voltage excites the stator beam across two electrodes on the left and right surfaces of the piezoceramics, these two equal potential surfaces have different electrical potentials. Therefore, the electrical boundary conditions of the electrical potential on the grounded electrode is set to zero. Moreover, for the ungrounded electrodes which have an electrical potential ϕ, the $\mathbf{F}_{Q_p}$ is the nodal charge on the ungrounded electrode surface. The electrical potential vector of the system can be set as [17]

$$\mathbf{Q}_\phi = \begin{Bmatrix} \mathbf{Q}_{\phi_i} \\ \mathbf{Q}_{\phi_p} \end{Bmatrix}, \tag{13}$$

where $\mathbf{Q}_{\phi_i}$ is the electrical potential vector corresponding to the internal nodes and $\mathbf{Q}_{\phi_p}$ is the electrical potential vector corresponding to the nodes on the ungrounded electrode surface. Then equation (12) can be partitioned correspondingly as

$$\begin{bmatrix} \mathbf{M}_{uu} & 0 & 0 \\ 0 & 0 & 0 \\ 0 & 0 & 0 \end{bmatrix} \begin{Bmatrix} \ddot{\mathbf{Q}}_u \\ \ddot{\mathbf{Q}}_{\phi_i} \\ \ddot{\mathbf{Q}}_{\phi_p} \end{Bmatrix} + \begin{bmatrix} \mathbf{K}_{uu} & \mathbf{K}_{u\phi_i} & \mathbf{K}_{u\phi_p} \\ \mathbf{K}_{u\phi_i}^{\mathrm{T}} & -\mathbf{K}_{\phi_i\phi_i} & -\mathbf{K}_{\phi_i\phi_p} \\ \mathbf{K}_{u\phi_p}^{\mathrm{T}} & -\mathbf{K}_{\phi_i\phi_p}^{\mathrm{T}} & -\mathbf{K}_{\phi_p\phi_p} \end{bmatrix} \begin{Bmatrix} \mathbf{Q}_u \\ \mathbf{Q}_{\phi_i} \\ \mathbf{Q}_{\phi_p} \end{Bmatrix} = \begin{Bmatrix} \mathbf{F}_F \\ 0 \\ \mathbf{F}_{Q_p} \end{Bmatrix}. \tag{14}$$

The first two sets of equation (14) can be rewritten as

$$\begin{bmatrix} \mathbf{M}_{uu} & 0 \\ 0 & 0 \end{bmatrix} \begin{Bmatrix} \ddot{\mathbf{Q}}_u \\ \ddot{\mathbf{Q}}_{\phi_i} \end{Bmatrix} + \begin{bmatrix} \mathbf{K}_{uu} & \mathbf{K}_{u\phi_j} \\ \mathbf{K}_{u\phi_i}^{\mathrm{T}} & -\mathbf{K}_{\phi_i\phi_i} \end{bmatrix} \begin{Bmatrix} \mathbf{Q}_u \\ \mathbf{Q}_{\phi_i} \end{Bmatrix} = \begin{Bmatrix} \mathbf{F}_F - \mathbf{K}_{u\phi_p}\mathbf{Q}_{\phi_p} \\ \mathbf{K}_{\phi_i\phi_p}\mathbf{Q}_{\phi_p} \end{Bmatrix}. \tag{15}$$

If $\mathbf{Q}_{\phi_p}$ is specified as the input for the resonator, the second set of equation (15) can be used to relate $\mathbf{Q}_{\phi_i}$ in terms of $\mathbf{Q}_{\phi_p}$. Then the first set of equation (15) can be rewritten as

$$\mathbf{M}_{uu}\ddot{\mathbf{Q}}_u + \mathbf{K}'_{uu}\mathbf{Q}_u = \mathbf{F}_F - \mathbf{F}_\phi, \tag{16}$$

where

$$\mathbf{K}'_{uu} = \mathbf{K}_{uu} + \mathbf{K}_{u\phi_i}\mathbf{K}^{-1}_{\phi_i\phi_i}\mathbf{K}^{\mathrm{T}}_{u\phi_i}, \tag{17}$$

$$\mathbf{F}_{\phi} = (\mathbf{K}_{u\phi_p} - \mathbf{K}_{u\phi_i}\mathbf{K}^{-1}_{\phi_i\phi_i}\mathbf{K}_{\phi_i\phi_p})\mathbf{Q}_{\phi_p}, \tag{18}$$

and $\mathbf{F}_{\phi}$ can be defined as the electrical force vector produced by the specified voltage vector at the piezoceramics. The last set of equation (14) can be used to calculate the charge distribution on the ungrounded electrode surfaces as long as equation (16) is solved.

Since the mechanical loss due to the viscoelasticity of the materials is an important factor for dynamic behavior of a vibration system, some damping effect has to be included in the model given in equation (16). The following form is introduced for simplifying the analysis

$$\mathbf{M}\ddot{\mathbf{Q}} + \mathbf{C}\dot{\mathbf{Q}} + \mathbf{K}\mathbf{Q} = \mathbf{F}, \tag{19}$$

where $\mathbf{M} = \mathbf{M}_{uu}$ and $\mathbf{K} = \mathbf{K}'_{uu}$ are the assembled system matrices, $\mathbf{Q} = \mathbf{Q}_u$ is the system nodal displacement vector and $\mathbf{F} = \mathbf{F}_F - \mathbf{F}_{\phi}$ is the external force. The damping matrix $\mathbf{C}$ added to the stator beam model in equation (16) is $\mathbf{C} = \alpha\mathbf{M}_{uu} + \beta\mathbf{K}'_{uu}$, where α and β are constants to be given.

2.3. NEW HYBRID LAPLACE TRANSFORM/FINITE ELEMENT METHOD

The governing equation (19) is a standard form of linear equation, which can be solved numerically by various numerical integration schemes. Here the new hybrid Laplace transform method [5, 6], instead of the Runge–Kutta method, is applied to increase the simulation efficiency.

One takes the Laplace transform with respect to equation (19) and obtains

$$(s^2\mathbf{M} + s\mathbf{C} + \mathbf{K})\bar{\mathbf{Q}} = \bar{\mathbf{f}}, \tag{20}$$

where $\bar{\mathbf{f}} = (s\mathbf{M} + \mathbf{C})\mathbf{Q}(0) + \mathbf{M}\dot{\mathbf{Q}}(0) + (1/s)\mathbf{F}$, s is a complex number, and $\bar{\mathbf{Q}}$ is a $(n \times 1)$ vector representing the unknown displacement functions of the Laplace transform.

Since $\mathbf{M}$ is positive definite, all of its eigenvalues are positive. One can define the following transform matrix:

$$\mathbf{R} = \left[\frac{\mathbf{e}_1}{\sqrt{\mu_1}}, \frac{\mathbf{e}_2}{\sqrt{\mu_2}}, \ldots, \frac{\mathbf{e}_n}{\sqrt{\mu_n}}\right], \tag{21}$$

where $\mathbf{e}_i$ is the ith eigenvector of $\mathbf{M}$ corresponding to its ith eigenvalue μ_i, and then the following transformed relation is obtained:

$$\mathbf{R}^{\mathrm{T}}\mathbf{M}\mathbf{R} = \mathbf{I}, \tag{22}$$

where $\mathbf{I}$ is the unit matrix. It is assumed that the eigenvalues are distinct. Sequentially, by using the following transformation,

$$\bar{\mathbf{Q}} = \mathbf{R}\bar{\mathbf{Q}}^{(1)}, \tag{23}$$

and pre-multiplying $\mathbf{R}$, equation (20) becomes

$$(s^2\mathbf{I} + s(\alpha\mathbf{I} + \beta\mathbf{G}) + \mathbf{G})\bar{\mathbf{Q}}^{(1)} = \bar{\mathbf{f}}^{(1)}, \tag{24}$$

where $\mathbf{G} = \mathbf{R}^{\mathrm{T}}\mathbf{K}\mathbf{R}$ and $\bar{\mathbf{f}}^{(1)} = \mathbf{R}^{\mathrm{T}}\bar{\mathbf{f}}$.

Now, $\mathbf{G}$ can be easily proved to be a symmetric matrix, and then it can be further reduced to a diagonal form. Setting

$$\bar{\mathbf{Q}}^{(1)} = \mathbf{P}\bar{\mathbf{Q}}^{(2)}, \tag{25}$$

where $\mathbf{P}$ is formed from the eigenvectors of $\mathbf{G}$ and $\mathbf{P}^{-t}\mathbf{P} = \mathbf{I}$, substituting equation (25) into equation (24) and pre-multiplying equation (24) by $\mathbf{P}^{-1}$ yield

$$(s^2\mathbf{I} + s(\alpha\mathbf{I} + \beta \cdot diag\,[\kappa_i]) + diag\,[\kappa_i])\bar{\mathbf{Q}}^{(2)} = \mathbf{P}^{-1}\bar{\mathbf{f}}^{(1)} = \bar{\mathbf{f}}^{(2)}, \tag{26}$$

where κ_i is the ith eigenvalue of matrix $\mathbf{G}$. Therefore, the following decoupled equations are obtained:

$$\{\bar{q}_i^{(2)}\} = \left\{\frac{\bar{f}_i^{(2)}}{s^2\mathbf{I} + s(\alpha\mathbf{I} + \beta \cdot diag\,[\kappa_i]) + diag\,[\kappa_i]}\right\}, \quad i = 1, 2, \ldots, n. \tag{27}$$

The inverse Laplace transform of $\bar{q}_i^{(2)}(s)$ can then be obtained by the partial fraction method. The merit of this proposed transformation is to deduce the decoupled form and the inverse Laplace transform solution can be obtained easily. Finally, the displacement $\bar{\mathbf{Q}}$ can be obtained by

$$\bar{\mathbf{Q}} = \mathbf{R}\mathbf{P}\bar{\mathbf{Q}}^{(2)}. \tag{28}$$

3. CONTACT OF STATOR WITH ROTOR

3.1. GEOMETRIC CONSTRAINT

When the beam tip comes into contact with the rotor, the position of the beam tip must satisfy the geometric constraint formed by its contact situation. Figure 3 shows the geometric relation between the beam tip position and the rotor. The position vector of the tip point B' after deformation is

$$\mathbf{R}_{OB'} = \mathbf{R}(l_t, 0, t) = (l_t + u_{N_e+1})\mathbf{i} + v_{N_e+1}\mathbf{j}. \tag{29}$$

The following relationship from the summation of vectors is valid:

$$\mathbf{R}_{OD} - \mathbf{R}_{OB'} = \mathbf{R}_{B'D}. \tag{30}$$

Using equations (29) and (30), we get the expression for vector $\mathbf{R}_{B'D}$. Since the magnitude of $\mathbf{R}_{B'D}$ is the radius of the rotor, the geometric constraint condition, when the beam tip touches the rotor, can be written as

$$C_B = (u_{N_e+1} - \delta)^2 - 2r(u_{N_e+1} - \delta) + v_{N_e+1}^2 = 0, \tag{31}$$

where δ is the gap from the undeformed beam tip to the rotor surface and r is the radius of the rotor. This algebraic equation must be satisfied during contact, which governs the motion of the tip point of the stator beam. Equation (31) implies that

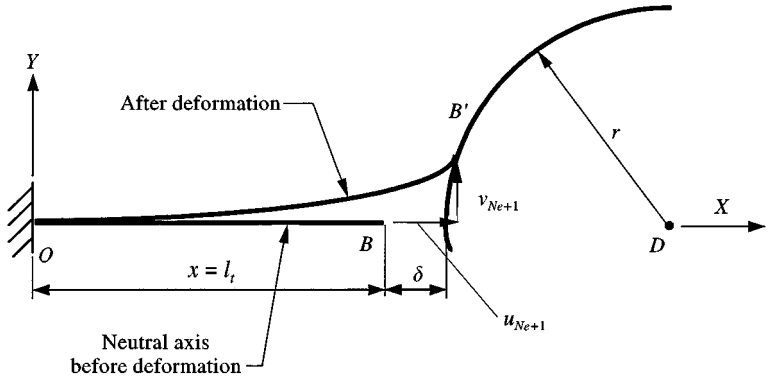

Figure 3. The initial and current state of the stator beam contacting with the rotor.

the longitudinal and transverse deflections at the beam tip are non-linearly coupled when the stator beam is in contact with the rotor. Furthermore, the friction force generated during contact is modeled by the coulomb friction law.

The Lagrange multiplier method is applied to treat the constrained dynamic problem, whereas the geometric condition is enforced by augmenting the Lagrange multiplier as an additional system variable. Following this approach, the external contact force vector $\mathbf{F}_F$ is calculated by means of two force terms. The first one is the generalized normal reaction force, which is calculated by the product of the scalar Lagrange multiplier with the gradient of the constraint, $\lambda \mathbf{B}^{\mathrm{T}}$, where $\mathbf{B} = [0, \ldots, \partial C_B/\partial u_{N_e+1}, \partial C_B/\partial v_{N_e+1}, 0]$. The second one is the generalized friction force $|\lambda| \mathbf{Q}_f^{\mathrm{T}}$, where $|\lambda|$ can be replaced by $\lambda \operatorname{sign} \lambda$, $\mathbf{Q}_f = \mu\{0, \ldots, \partial C_B/\partial v_{N_e+1}, -\partial C_B/\partial u_{N_e+1}, 0\}$, and μ is the dynamic friction coefficient. Then the constrained dynamic equations can be rewritten from equation (19) as the following one:

$$\ddot{\mathbf{Q}}_u = \mathbf{M}_{uu}^{-1}[-\mathbf{C}\dot{\mathbf{Q}}_u - \mathbf{K}'_{uu}\mathbf{Q}_u + \lambda(\mathbf{B}^{\mathrm{T}} + \mathbf{Q}_f^{\mathrm{T}} \operatorname{sign} \lambda) - \mathbf{F}_\phi]. \tag{32}$$

The positive rotation direction of the rotor is defined in the counterclockwise direction, while the positive direction of friction force F_t is defined as the one which makes the rotor rotate counterclockwise. This definition allows us to write the equation of the revolution of the rotor in the form:

$$J\ddot{\theta} + C_d\dot{\theta} = rF_i - M_p \tag{33}$$

where J is the moment of inertia of the rotor, C_d is the viscous damping constant and M_p is the prescribed torque. The normal contact force F_n can be determined from $\lambda \mathbf{B}^{\mathrm{T}}$, while the friction force F_t can be determined from $\lambda \mathbf{Q}_f^{\mathrm{T}} \operatorname{sign} \lambda$.

3.2. NUMERICAL SCHEME FOR CONSTRAINED MOTION

To solve the constrained dynamic system of the mixed differential-algebraic equations formed by equations (31) and (32), the numerical technique proposed by Hatman *et al.* [18] is used. The numerical algorithm for the entire problem can be

found in reference [16]. The numerical scheme is summarized as follows: (1) If t_{n-1}, $\mathbf{Q}_{u,n-1}$ and $\dot{\mathbf{Q}}_{u,n-1}$ are known, predict values $\mathbf{Q}^p_{u,n}$ and $\dot{\mathbf{Q}}^p_{u,n}$ at t_n. (2) By using the backward difference method (BDF) and the Newton–Raphson iterative method to solve the corrected values, the generalized co-ordinates can be computed as

$$\mathbf{Q}_{u,n} = \mathbf{Q}_{u,n-1} + t_h \dot{\mathbf{Q}}^p_{u,n} + \frac{C_B(\mathbf{Q}^p_{u,n}, t_n)}{\mathbf{B}(\mathbf{Q}^p_{u,n}, t_n) \cdot \mathbf{B}^{\mathrm{T}}(\mathbf{Q}^p_{u,n}, t_n)} \mathbf{B}^{\mathrm{T}}(\mathbf{Q}^p_{u,n}, t_n), \tag{34}$$

where t_h is the constant time step. (3) Using a similar BDF method, the corrected generalized velocities are computed by

$$\begin{aligned}\dot{\mathbf{Q}}_{u,n} = \dot{\mathbf{Q}}_{u,n-1} - t_h \mathbf{M}^{-1}_{uu} \cdot \mathbf{K}'_{uu} \cdot \mathbf{Q}_{u,n} + t_h \lambda_n \mathbf{M}^{-1}_{uu} \cdot \mathbf{B}^{\mathrm{T}}(\mathbf{Q}_{u,n}, t_n) \\ + t_h \lambda_n \operatorname{sign}(\lambda_n) \mathbf{M}^{-1}_{uu} \cdot \mathbf{Q}^{\mathrm{T}}_f(\mathbf{Q}_{u,n}, \dot{\mathbf{Q}}^p_{u,n}, t_n) - t_h \mathbf{M}^{-1}_{uu} \mathbf{F}_\phi,\end{aligned} \tag{35}$$

where λ_n is the value of the Lagrange multiplier at time t_n, and can be calculated by substituting equation (35) into equation (32), i.e.

$$\lambda_n = \frac{t_h \mathbf{B}(\mathbf{Q}_{u,n}, t_n) \cdot \mathbf{M}^{-1}_{uu} \cdot \mathbf{K}'_{uu} \cdot \mathbf{Q}_{u,n} - \mathbf{B}(\mathbf{Q}_{u,n}, t_n) \cdot \dot{\mathbf{Q}}_{u,n-1} + t_h \mathbf{B}(\mathbf{Q}_{u,n}, t_n) \cdot \mathbf{M}^{-1}_{uu} \cdot \mathbf{F}_\phi}{t_h \mathbf{B}(\mathbf{Q}_{u,n}, t_n) \cdot \mathbf{M}^{-1}_{uu} \cdot [\mathbf{B}^{\mathrm{T}}(\mathbf{Q}_{u,n}, t_n) + \mathbf{Q}^{\mathrm{T}}_f(\mathbf{Q}_{u,n}, t_n) \operatorname{sign}(\lambda_n)]}. \tag{36}$$

(4) Put $\mathbf{Q}^p_{u,n} = \mathbf{Q}_{u,n}$ and $\dot{\mathbf{Q}}^p_{u,n} = \dot{\mathbf{Q}}_{u,n}$ and repeat (2) and (3) until the value λ_n does not change. (5) Go to step 1 to simulate the next time step.

4. NUMERICAL RESULTS AND DISCUSSIONS

Transient responses of the piezoelectric beam without and with rotor are analyzed by the new hybrid Laplace transform/finite element method in this section and the results are compared with those obtained by the Runge–Kutta method. The material properties of the stator beam are listed in Table 1. The rotor is made of steel, with a thickness of 2·5 mm and a radius $r = 20$ mm, which is assumed to be rigid. Due to the slender geometry of the beam structure, the axial and bending stiffness are quite small compared to that of the rotor. The assumption of the rigid rotor should be a reasonable approximation.

The coefficient of the dry friction μ between the rotor and stator beam and the shape factor K for the beam are taken to be 0·2 and 0·85 respectively. The input voltage applied to the piezoceramics is

$$V_t = V_l \sin\left(2\pi \frac{f}{2} t\right) + V_f \sin(2\pi f t + \Theta), \tag{37}$$

where f is the exciting frequency for the bending mode, Θ is the phase displacement and the V_l and V_f are the voltage amplitudes. The two constants in the beam damping model $\alpha = 0{\cdot}002$ and $\beta = 1 \times 10^{-7}$ are used, while the damping constant of the rotor $C_d = 0{\cdot}0002$ is chosen. The damping constants used in simulation are only for proper demonstration. For actual application, these values can be determined by usual methods from vibration theory and experimentation. The

TABLE 1

Material properties and dimensions of the piezoelectric stator

	Steel	Piezoceramics	Aluminum
Young's Modulus E (Gpa)	220	63·0	70
Poisson's ratio v	0·3	0·3	0·33
Shear Modulus G (GPa)	84·6	24·2	26·3
Density ρ (kg/m^3)	7800	7600	2710
Piezoelectric (C/m^2)			
e_{111}	0	16·0	0
e_{112}	0	36·8	0
Dielectric ε^s_{11} (nN/V^2)	0	15·3	0
Length l (mm)	$l_s = 20$	$l_l = 7{\cdot}5$ $l_f = 7{\cdot}5$	$l_a = 45$
Width b (mm)	$b_s = 24$	$b_l = 15$ $b_f = 15$	$b_a = 15$
Depth h (mm)	$h_s = 24$	$h_l = 15$ $h_f = 7{\cdot}5$	$h_a = 4$ or 12

TABLE 2

Comparison between the natural frequencies (Hz) *of the cantilever beam*

Mode	Only aluminum $h_a = 4$ mm	Stator beam $h_a = 4$ mm	Stator beam $h_a = 12$ mm
v(I)	1621·73	1573·38	3018·62
v(II)	10163·23	9098·90	13096·00
v(III)	28457·34	17219·01	24338·12
v(IV)	55765·04	29556·44	36718·75
u(I)	28235·27	24032·38	19033·81

Note: v(I): first bending mode, v(II): second bending mode, v(III): third bending mode, v(IV): fourth bending mode, u(I): first axial mode

simulations are done on a personal computer with the Intel Pentium 166 MHz. When the Runge–Kutta method in MATLAB is used, the desired accuracy 10^{-9} is specified and the integration time step is 1 μs for the Runge–Kutta method. Without specially notifying the element number in the following simulations, an eight-element model, two elements for each part of the beam, are used.

4.1. TRANSIENT RESPONSES WITHOUT ROTOR

In Table 2, the natural frequencies for different stator beam designs are computed by solving the eigenvalue problem formed by equation (16). To have a beam resonator with its fourth bending natural frequency being two times its first axial natural frequency, a simplified design is used in which only the aluminum beam is considered and the classical beam formulation of natural frequency is applied.

Some calculated natural frequencies are shown in the first column of Table 2. Then transient responses of the piezoelectric resonator are simulated with $f = 55765$ Hz, $V_l = 200$ V, $V_f = 300$ V, $\Theta = 0$ and the results are simulated with time step 1 μs for this hybrid method. In Figures 4(a) and (b) the axial and bending deflections at the beam tip are shown respectively. In these two figures beating phenomena and the damping effect can be seen. Finally, the steady state response is obtained. The trajectory of beam tip during the time range $3\text{ ms} \leqslant t \leqslant 5\text{ ms}$ is shown in Figure 4(c), and a distorted Lissajous figure is formed. The external excitation voltage is shown in Figure 4(d). This is because the input voltage with $f/2$ frequency used to stimulate the axial vibration also excites certain amount of the bending vibrations with this frequency, as shown in Figure 4(b). It can be seen obviously from beam frequencies shown in Table 2 that the real natural frequencies in column two of the stator beam are quite different from the simple model in column one. The

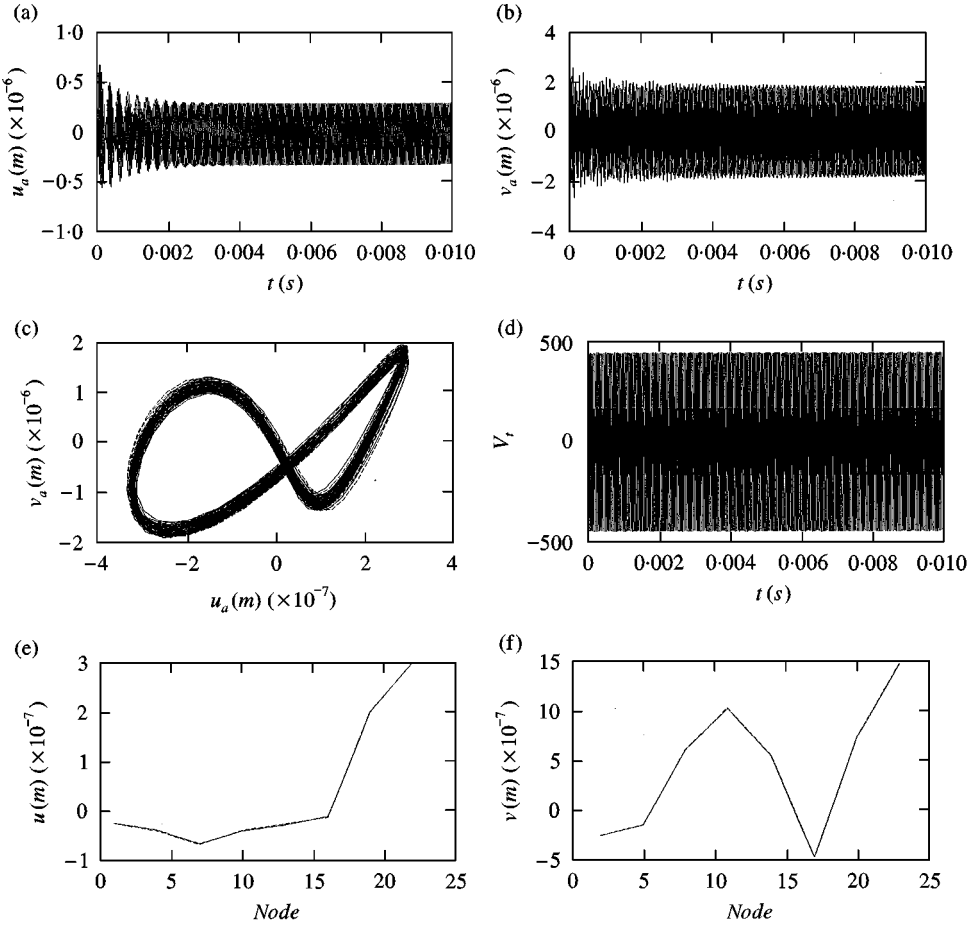

Figure 4. The transient axial and transverse amplitudes of the stator beam for the forced vibration with $f = 55765$ Hz and $h_a = 4$ mm. (a) Axial deflection u_a, (b) transverse deflection v_a, (c) trajectory at beam tip during $3\text{ ms} \leqslant t \leqslant 5$ ms, (d) the external excitation voltage, (e) the nodal axial deflection u at $t = 3$ ms, (f) the nodal transverse deflection v at $t = 3$ ms.

natural frequency of the fourth bending mode of the piezoelectric beam with $h_a = 4$ mm is 29556 Hz which is close to the $f/2$. This is why certain bending vibrations with $f/2$ frequency is stimulated. If the beam tip follows the sharp geometry at the right end of the tip trajectory, as in Figure 4(c), and if the rotor is put into its place to be driven by the beam tip, it will certainly yield bad performance. Thus, a more accurate design is needed.

The numerical simulations in Figures 4(e) and (f) show the nodal displacements obtained by the new method,which are almost identical with those obtained by the Runge-Kutta method. The computation time, for these results until $t = 3$ ms, by use of the new method (-.-.-.), is 965 s, which is about eight times faster than 8117 s by the Runge–Kutta method (—). From this simple case, the hybrid method saves a lot of computation time and shows its superior effectiveness over the Runge–Kutta method.

A new height of the aluminum beam is designed based on the piezoelectric beam model. Through several tries, new height of $h_a = 12$ mm is chosen and the new set of natural frequencies can be found in the third column of Table 2. With this new design the fourth bending frequency 36719 Hz is almost twice the first axial frequency 19034 Hz. A new input voltage frequency $f = 36\,000$ Hz is applied to stimulate this redesign. Figures 5(a)–(c) show the transient responses and similar behavior as that in Figures 4(a)–(c). However, the tip trajectory shown in Figure 5(c) with the same time period is much smoother than the first design. Another simulation with input voltage frequency $f = 38\,000$ Hz, which is also close to the fourth bending frequency 36719 Hz, is performed and the results are shown

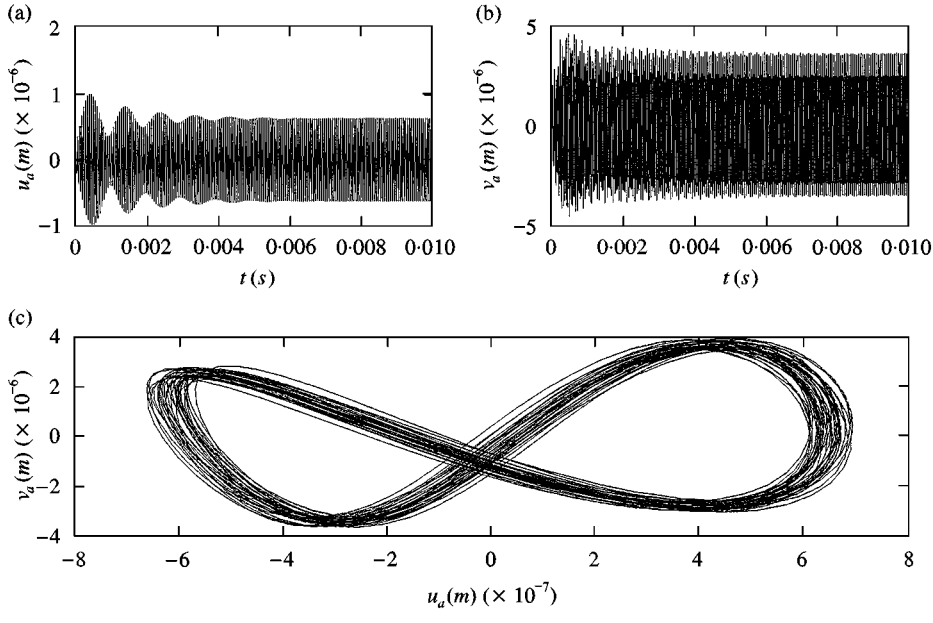

Figure 5. The transient axial and transverse amplitudes of the stator beam for the forced vibration with $f = 36000$ Hz and $h_a = 12$ mm. (a) Axial deflection u_a, (b) transverse deflection v_a, (c) trajectory at beam tip during 3 ms $\leqslant t \leqslant$ 5 ms.

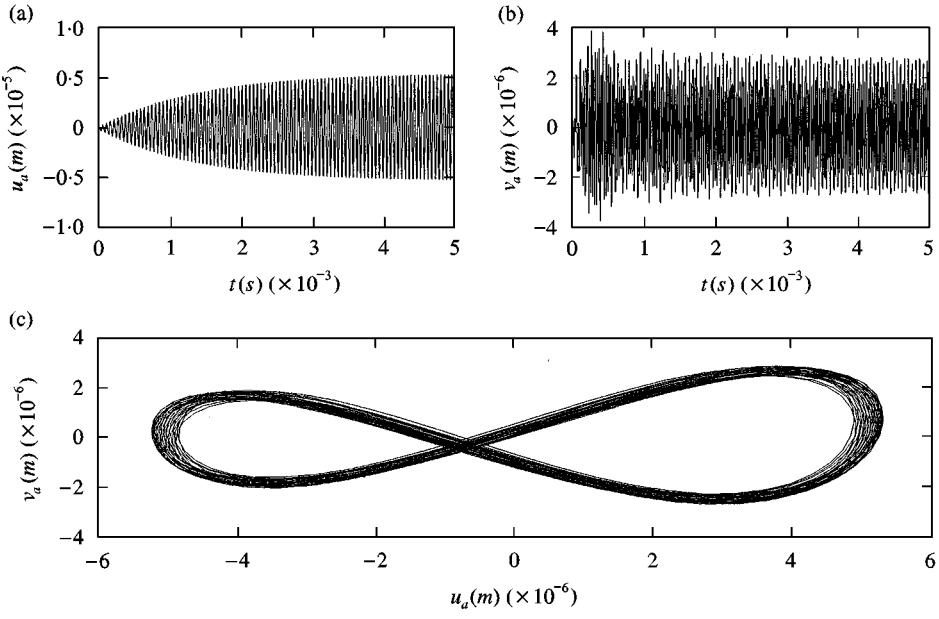

Figure 6. The transient axial and transverse amplitudes of the stator beam vibration with $f = 38000$ Hz and $h_a = 12$ mm. (a) Axial deflection u_a, (b) transverse deflection v_a, (c) trajectory at beam tip during 3 ms $\leqslant t \leqslant$ 5 ms.

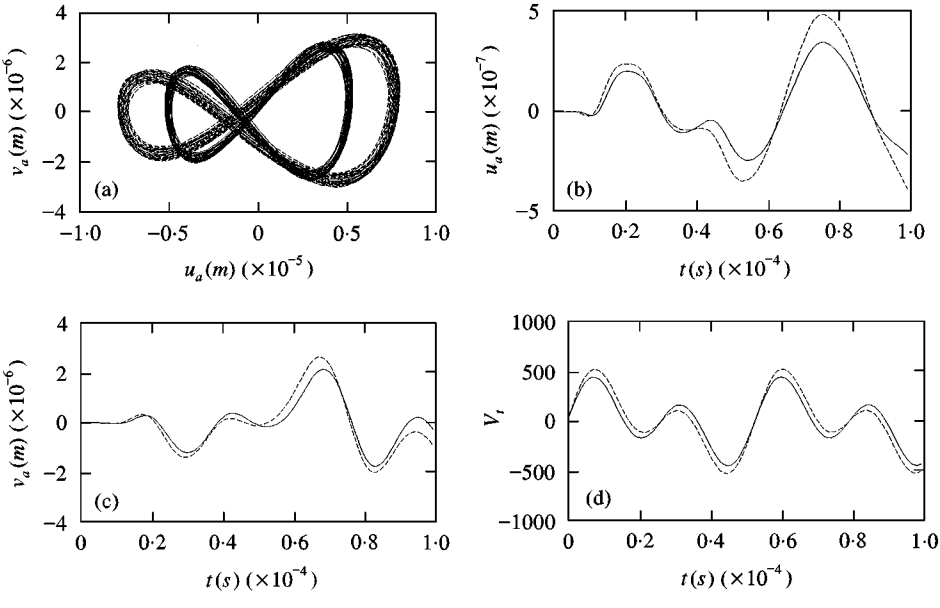

Figure 7. The transient axial and transverse amplitudes of the stator beam vibration with $f = 38000$ Hz and $h_a = 12$ mm with different input voltages V_l (— 200 V, … , 300 V).

in Figures 6(a)–6(c). In Figure 6(a) the beating phenomenon disappears and the amplitude gradually increases. Smooth trajectory is also shown in Figure 6(c).

Figures 7 and 8 show the effect of different voltage amplitude and phase of the input voltage of equation (37) on the transient responses. It is observed in Figure 7

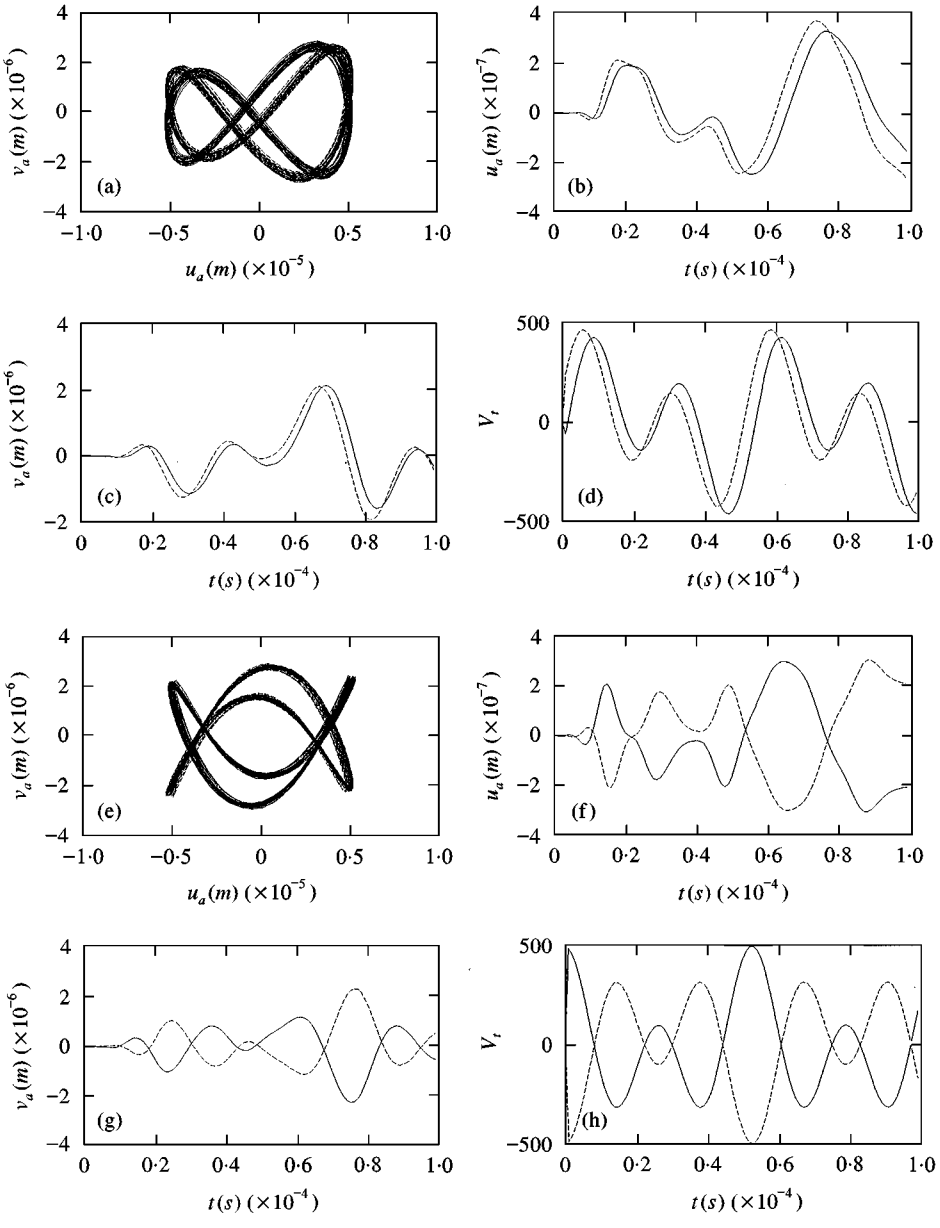

Figure 8. The transient axial and transverse amplitudes of the stator beam vibration with $f = 38000$ Hz and $h_a = 12$ mm. In (a)–(d), Θ $(-0{\cdot}1\,\pi, \ldots, -0{\cdot}1\,\pi)$, (a) trajectory at beam tip during 3 ms $\leqslant t \leqslant$ 5 ms, (b) axial deflection u_a, (c) transverse deflection v_a, (d) the external voltage. In (e)–(h), Θ $(-0{\cdot}5\,\pi, \ldots, -0{\cdot}5\,\pi)$, (e) trajectory at beam tip during 3 ms $\leqslant t \leqslant$ 5 ms, (f) axial deflection u_a, (g) transverse deflection v_a, (h) the external voltage.

that the axial amplitude is larger when the amplitude of axial voltage is increased. Figure 8 shows Lissajous figures for the different phases of input voltage. The results in Figures 4–8 show that different trajectories can be adjusted by changing the exciting frequency, amplitude and phase of the input voltage to yield better performance.

4.2. TRANSIENT RESPONSES WITH ROTOR

In order to study the dynamic performance of the bimodal motor, the contact between the stator beam and the rotor must be considered. The mixed differential–algebraic equations (31) and (32) are solved to obtain the transient responses. Some numerical simulations are performed under the same driving condition as used in Figure 6. Three different gaps between the undeformed beam tip and the rotor shown in Figure 3, i.e., $\delta = 3, 4$ and 4.5 μm, are set and the resulting performance is simulated and compared. Since the axial amplitude of the steady state response shown in Figure 6(a) is about 5 μm, the rotor is placed at a position such that the gap δ must fall below this value in order to come into contact with each other. As the axial deflection in this case increases monotonously, the beam tip is expected to touch the rotor. Figures 9(a)–(d) show the results for $\delta = 3$ mm. Figure 9(a) shows the transient responses of axial deflection and the constraint is satisfied as predicted. The rotor velocity history driven by the contact friction force is shown in Figure 9(b). Figure 9(c) shows the tip trajectory. From Figure 9(c) it is seen that the final steady trajectory is very different from the Lissajous trajectory without contact, as shown in Figure 6(c). The induced contact force is shown in Figure 9(d). The results of the initial gap of 4 and 4·5 μm are shown in Figures 10 and 11 respectively. From the normal contact force histories shown in Figures 9(d), 10(d) and 11(d), it reveals that not every oscillating period of the beam comes into contact with the rotor. For this range of gap, more often the contact and lower normal contact force occurs as the gap distance decreases. The

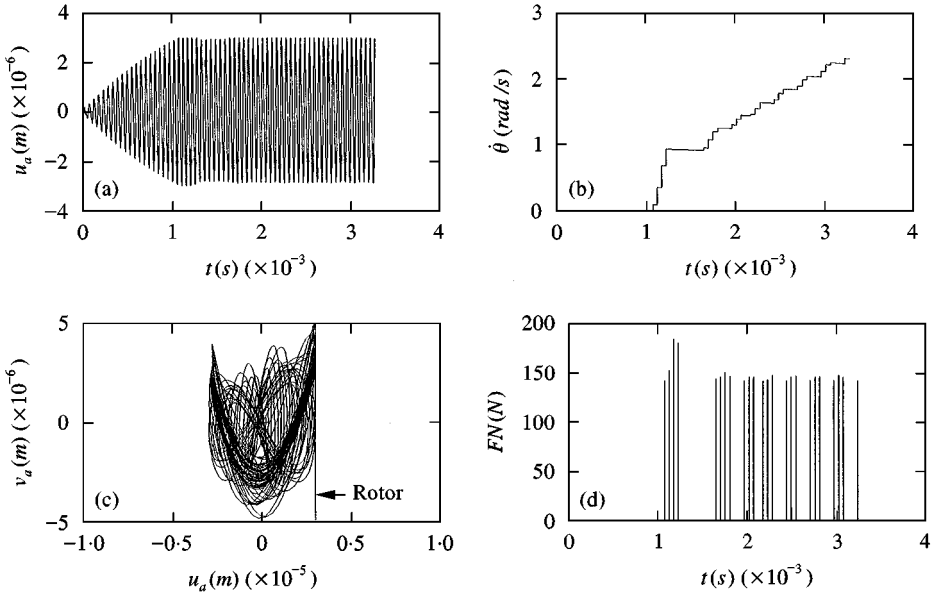

Figure 9. Transient responses with contacting rotor with $f = 38\,000$ Hz, $h_a = 12$ mm and $\delta = 3$ μm. (a) Axial deflection u_a, (b) rotor velocity $\dot{\theta}$, (c) trajectory of beam tip, (d) normal contact force.

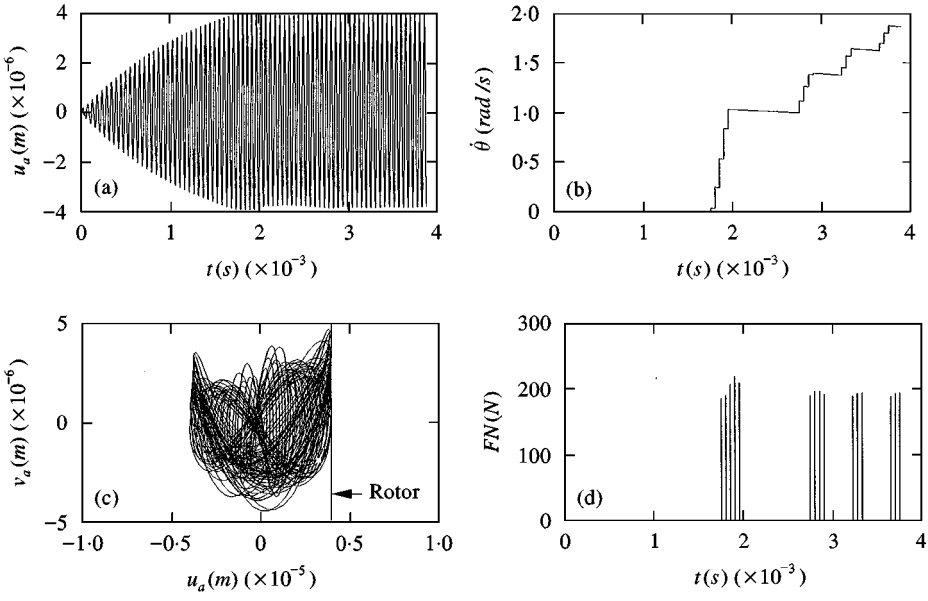

Figure 10. Transient responses with contacting rotor with $f = 38\,000$ Hz, $h_a = 12$ mm and $\delta = 4$ μm. (a) Axial deflection u_a, (b) rotor velocity $\dot{\theta}$, (c) trajectory of beam tip, (d) normal contact force.

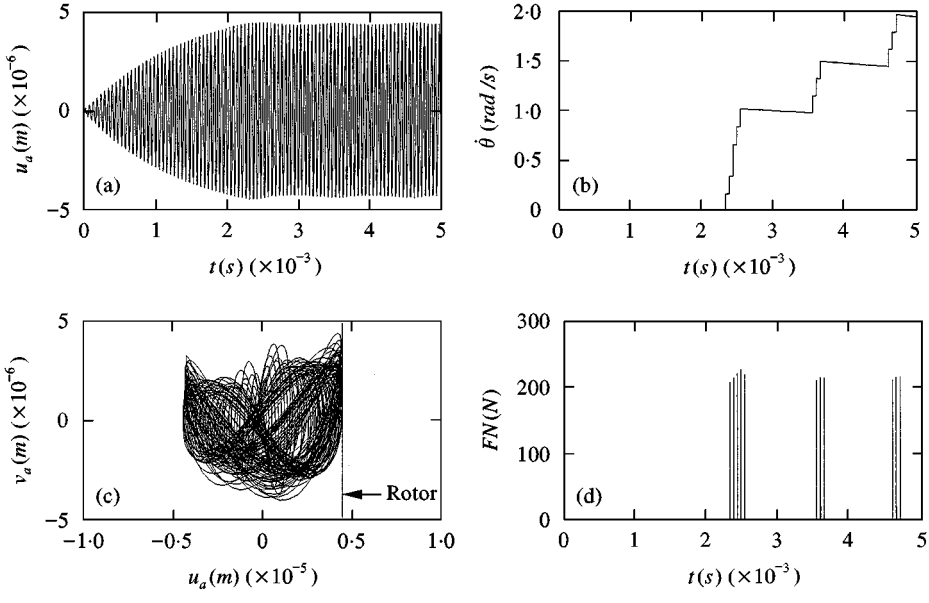

Figure 11. Transient responses of contacting rotor with $f = 38\,000$ Hz, $h_a = 12$ mm and $\delta = 4.5$ μm. (a) Axial deflection u_a, (b) rotor velocity $\dot{\theta}$ (c) trajectory of beam tip, (d) normal contact force.

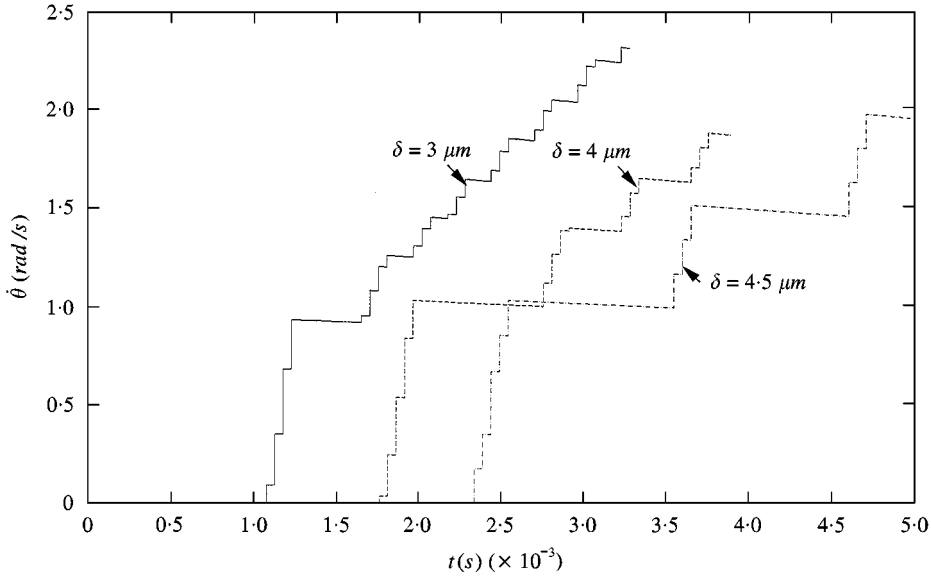

Figure 12. Histories of rotor velocities at different, $\delta = 3$ μm (——), 4 μm (– – –), 4·5 μm (·····).

rotating velocities of the rotor for these three cases are put together and compared in Figure 12. It is obvious that $\delta = 3$ μm is a better design and has a quicker start-up and a better rotary acceleration.

5. CONCLUSION

In this paper the governing equations for the piezoelectric beam are formulated by the finite element method, which describe the dynamic behavior of the stator beam when the electrode voltage is applied. Then the contact condition is treated and a numerical scheme is applied to simulate the dynamic contact behavior. During operation of the bimodal motor, contact and without contact with the rotor for forced vibration of the piezoelectric beam will alternately occur. Thus the rotor accelerates only when the beam tip touches the rotor surface. The new hybrid Laplace transform/finite element method is applied to greatly increase the simulation speed for transient responses. Using the transform method on the matrix with complex-number coefficients, this hybrid method can be used to handle problems with many nodes. As there is no restriction on integration time step to ensure accuracy for this method, many fewer points are needed to be computed between adjacent contact periods, hence saving much computing time. Some of the results are also compared with those of the Runge–Kutta method.

From the numerical simulations, some conclusions are drawn as follows:

(1) The new hybrid Laplace transform/finite element method combined with a similarity transform method can indeed speed up the computation time for

the bimodal motor, in which the differential–algebraic equations govern the contact behavior.

(2) The stator beam should be designed properly to have suitable natural frequencies such that better tip trajectory can be formed. Proper turning the amplitudes, phase angle and exciting frequencies of input voltage may yield a better design.

(3) Interaction between stator beam and rotor due to contact may influence the trajectory of the beam tip dramatically. Thus in order to design a bimodal motor having better performance, the simulation of contact behavior should be conducted. The proposed method can be used to solve numerically this dynamic behavior.

(4) The gap between the beam tip and rotor is also an important factor, which should be carefully addressed to yield better performance.

ACKNOWLEDGMENT

The authors are greatly indebted to the National Science Council of the R.O.C. for the support of the research through contract No. NSC-87-2212-E-033-016.

REFERENCES

1. H. T. Chen and C. K. Chen 1988 *Numerical Heat Transfer* **14**, 343–356. Application of hybrid Laplace transform/finite-difference method to transient heat conduction problems.
2. H. T. Chen and C. K. Chen 1988 *International Journal for Numerical Methods in Engineering* **26**, 1433–1447. Hybrid Laplace transform/finite difference method for transient heat condition problems.
3. T. M. Chen 1992 *Computer Methods Applied Mechanics & Engineering* **98**, 261–272. A modified hybrid Laplace transform/finite element methods for transient heat conduction problems.
4. H. T. Chen, T. M. Chen and C. K. Chen 1987 *Computer Methods Applied Mechanics & Engineering* **63**, 83–85. Hybrid Laplace transform/finite element method for one-dimensional transient heat conduction problems.
5. C. K. Chen and T. M. Chen 1991 *Numerical Heat Transfer Part B* **20**, 191–205. New hybrid Laplace transform/finite element method for two-dimensional transient heat conduction problem.
6. C. K. Chen and T. M. Chen 1991 *International Journal for Numerical Methods in Engineering* **32**, 45–61. New hybrid Laplace transform/finite element method for three-dimensional transient heat conduction problem.
7. H. T. Chen and J. Y. Lin 1991 *International Journal of Heat Mass Transfer* **34**, 1301–1308. Hybrid Laplace transform technique for non-linear transient thermal problems.
8. T. M. Chen 1995 *International Journal for Numerical Methods in Engineering* **38**, 509–522. The hybrid Laplace transform/finite element method applied to the quasi-static and dynamic analysis of viscoelastic Timoshenko beams.
9. F. Durbin 1973 *Computer Journal* **17**, 371–376. Numerical inversion of Laplace transforms: efficient improvement to Dubner and Abate's method.
10. G. Honig and U. Hirdes 1984 *Journal of Computer Applied Mathematics* **9**, 113–132. A method for the numerical inversion of Laplace transform.

11. M. Fleischer, D. Stein and H. Meixner 1989 *IEEE Transactions on Ultrasonics, Ferroelectrics, and Frequency Control* **36**, 607–613. Ultrasonics piezomotor with longitudinally oscillating amplitude-transforming resonator.
12. M. Fleischer, D. Stein and H. Meixner 1989 *IEEE Transactions on Ultrasonics. Ferroelectrics, and Frequency Control* **36**, 614–619. New type of piezoelectric ultrasonic motor.
13. M. Fleischer, D. Stein and H. Meixner 1990 *Sensors and Actuators* **A21–A23**, 357–361. Novel ultrasonic motors with mono- and bimodal drives.
14. S. K. Ha, C. Keilers and F. K. Chang 1992 *AIAA Journal* **30**, 772–780. Finite element analysis of composite structures containing distributed piezoceramic sensors and actuators.
15. M. A. Moetakef, K. L. Lawrence, S. P. Joshi and P. S. Shiakolas 1995 *American Institute of Aeronautics and Astronautics Journal* **33**, 136–142. Closed-form expressions for higher order electroelastic tetrahedral elements.
16. R. F. Fung, C. M. Yao and D. G. Chang 1999 *IEEE Transactions on Ultrasonic, Ferroelectrics, and Frequency Control* **46**, 47–60, Dynamic and contact analysis of a bimodal ultrasonic motor.
17. N. Guo and P. Cawley 1992 *Journal of Sound and Vibration* **159**, 115–138. January. The finite element analysis of the vibration characteristics of piezoelectric discs.
18. V. G. Hatman, I. Haque and A. Bagchi 1996 *Journal of Sound and Vibration* **194**, 653–669. Dynamics of a flexible rotating beam interacting with a flat rigid surface, Part I: model development.

APPENDIX: NOMENCLATURE

A	cross-sectional area of the beam
b	width
C_d	viscous damping
D_i	electric displacement
E_k	electric field
e_{ij}	piezoelectric constant
$\mathbf{F}_F^*$	applied force
h	depth
$\mathbf{i}, \mathbf{j}$	unit vectors in the X and Y directions respectively
I	area moment of inertia about neutral axis
J	moment of inertia of a rotor
K	shape factor
l_p	length of piezoceramics
l_t	length of stator beam (total length)
l_e	length of an element
r	radius of rotor
S_{ij}	strain field
T_e	kinetic energy of an element
t	time
t_h	constant time step
U_e	strain energy of an element
u, v	longitudinal and transverse displacements respectively
V	volume
V_t	input voltage
OXY	global co-ordinate system
ρ	mass density
λ	Lagrange multiplier
f	exciting frequency

θ angle of rotor
Θ phase angle
ε_{ij} dielectric constant
ψ rotation angle of Timoshenko beam
ϕ electric potential
μ coefficient of dry friction
δ gap between the undeformed beam and rotor